J. Fluid Mech. (1984), *vol.* 147, *pp.* 291–313
Printed in Great Britain

Shallow flow over an isolated obstacle

By V. R. LAMB

Department of Marine, Earth and Atmospheric Sciences, North Carolina State University, Raleigh, North Carolina 27650

AND R. E. BRITTER

Department of Engineering, University of Cambridge, England

(Received 7 September 1982 and in revised form 25 May 1984)

This is a study of how certain geometrical and flow parameters affect the tendency of a fluid to flow around rather than over a single obstacle of simple shape in a homogeneous non-rotating fluid. A series of numerical experiments was conducted with a finite-difference model of such a shallow flow, assuming a hydrostatic pressure distribution. The results demonstrate how the flow over a three-dimensional obstacle deviates from the patterns established for a two-dimensional ridge. Measures are suggested for quantitative assessment of the tendency to flow around as a function of relative hill height and Froude number.

A series of laboratory experiments was also performed, examining the motions of two superposed homogeneous layers of fluid past an isolated obstacle in a towing tank. The resulting motion of the interface was found to agree with the results of the numerical experiments. The laboratory experiments also extended the understanding gained from the numerical experiments. Flow-visualization techniques were employed to aid in the qualitative assessment of the flow around the obstacles and its dependence on hill and flow parameters. In particular, these techniques demonstrated the impingement of the interface on the obstacle, and its dependence on flow speed and hill height.

1. Introduction

The determination of flow patterns over and around obstacles is a problem of great current interest. One important application is that of the prediction of surface concentrations due to pollutant plumes in complex terrain. In this problem, for a stably stratified atmosphere, where the boundary layer is very shallow and the plume is above the boundary layer, the flow governing the plume motion can be considered inviscid, affected by the terrain only through the deformation of the lower boundary. In this and other examples, the final goal is one of predicting stably stratified flow with wind shear over complex terrain. The present study represents a first step toward this goal by confirming and extending our knowledge of a homogeneous atmosphere with constant mean wind over an isolated obstacle.

Often, topographic features of a height large enough to protrude through the boundary layer are of a horizontal scale large enough that the hydrostatic approximation can be justified for the topographically induced motions. The numerical experiments presented here concentrate on such hydrostatic motions in a single layer

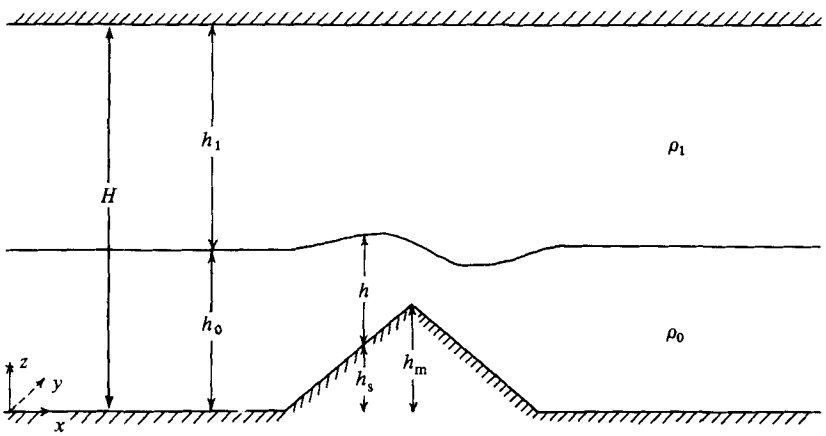

FIGURE 1. Diagram showing notation for one- and two-layer model.

of non-rotating homogeneous incompressible fluid with a free surface, governed by the following equations:

$$\frac{\partial u}{\partial t}+u\frac{\partial u}{\partial x}+v\frac{\partial u}{\partial y}=-g\frac{\partial}{\partial x}(h+h_s), \tag{1a}$$

$$\frac{\partial v}{\partial t}+u\frac{\partial v}{\partial x}+v\frac{\partial v}{\partial y}=-g\frac{\partial}{\partial y}(h+h_s), \tag{1b}$$

$$\frac{\partial h}{\partial t}+\frac{\partial}{\partial x}(hu)+\frac{\partial}{\partial y}(hv)=0, \tag{1c}$$

where u, v are the velocity components in the x-, y-directions respectively, h is the fluid depth, and the bottom topography is defined by $h_s(x, y)$, as shown in the lower layer of figure 1. This model is a useful one for, although highly simplified, the nonlinear effect in the advective terms is retained. For several special cases, the equations yield analytic solutions that can act as guides. In addition, since the motion is independent of the height coordinate, a finite-difference model for the equations can be integrated in time rather easily to obtain solutions in more general cases.

Previous numerical studies have concentrated, for the most part, on the case with no cross-stream dependence. The analysis of the possibly steady solutions of (1) for a two-dimensional obstacle and flow is now well known (see e.g. Long 1972; Baines & Davies 1980). Briefly, for steady flow over a ridge (1*a–c*) become

$$\frac{\partial}{\partial x}[\tfrac{1}{2}u^2+g(h+h_s)]=0, \tag{2a}$$

$$\frac{\partial}{\partial x}(hu)=0, \tag{2b}$$

so that both the quantity $\frac{1}{2}u^2+g(h+h_s)$ and the mass flux $Q\equiv hu$ must be constant throughout the fluid, fixed by the initial values h_0, u_0. If the specific energy e is defined as the sum of kinetic and potential energy per unit mass,

$$e\equiv\frac{u^2}{2g}+h=\frac{Q^2}{2gh^2}+h, \tag{3}$$

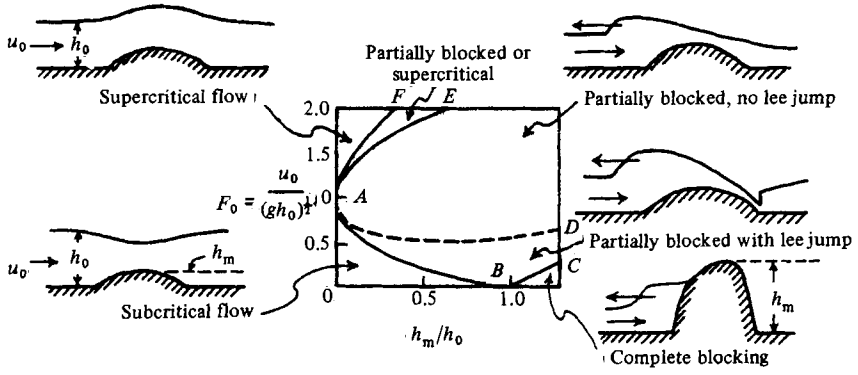

FIGURE 2. Curve FAB defined by condition that $F = 1$ at crest of ridge obstacle, differentiating regions where continuous steady-state solutions can exist (from Baines & Davies 1980).

then (2a) gives
$$\frac{\partial e}{\partial x} = -\frac{\partial h_s}{\partial x}, \tag{4}$$

so the flow loses and then gains specific energy as it moves up the obstacle and then down the lee side. It can be shown from (3) that for given Q a critical value of e is attained where $h = u^2/g$, called the critical depth; depths less than and greater than this are termed supercritical and subcritical respectively. If the maximum value, h_m, of h_s is large enough that, according to (4), the specific energy must drop below the critical value as it passes over the obstacle, it is concluded that no steady solution exists for such h_m and Q. The critical solutions are thus defined by the curve derived from (2a) representing values of u_0, h_0 and h_m where $u^2 = gh$ at the crest of the hill:

$$F_0^2 - 3F_0^{\frac{2}{3}} = 2(h^* - 1), \tag{5}$$

where $F_0 \equiv u_0/(gh_0)^{\frac{1}{2}}$, the Froude number of the initial state, and $h^* \equiv h_m/h_0$. The curve of F_0 versus h^* given by (5) is shown in figure 2 as FAB (figure from Baines & Davies 1980).

The possible configurations of surface height for the regimes shown in figure 2 were derived as solutions of steady equations. That these solutions correspond to long-term solutions of the time-dependent equations has been verified in a few cases with numerical models (Houghton & Kasahara 1968; Larsen 1966) and with flow-tank experiments (Long 1954). Thus, for the two-dimensional case, the flow pattern can be considered to be determined by the two dimensionless parameters F_0 and h^*.

If a three-dimensional obstacle is substituted for the ridge, the following form of the momentum equation (1) for steady flow applies:

$$(\nabla_H \times v_H) \times v_H + \nabla_H[\tfrac{1}{2}v_H^2 + g(h + h_s)] = 0. \tag{6}$$

Along each streamline we can write

$$\tfrac{1}{2}v_H^2 + g(h + h_s) = E_0, \tag{7}$$

where E_0 is a constant specified in the absence of a disturbance, and from this we define the two-dimensional Froude number

$$F \equiv \left(\frac{v_H^2}{gh}\right)^{\frac{1}{2}}. \tag{8}$$

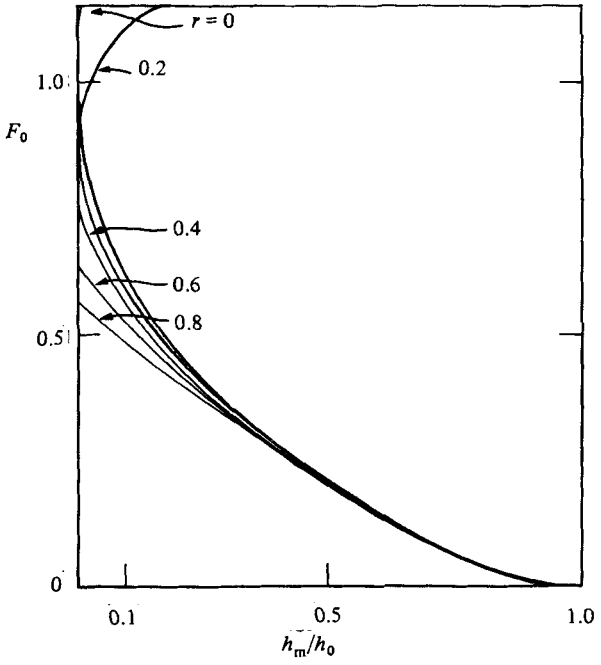

FIGURE 3. Curve defined by condition that $F = 1$ at crest of ridge obstacle for different values of r, relative depth of lower layer (from Baines & Davies 1980).

If $F = 1$ at the crest again defines critical flow, a curve analogous to that of figure 2 should exist. An analytic expression for such a critical curve is not available, but it should be possible to determine the curve through numerical experiments in which finite-difference analogues of (1) are integrated to an asymptotic state. At present, however, non-rotating shallow flow over and around three-dimensional obstacles has been studied through initial-value experiments only minimally. On the basis of a repetition of Houghton & Kasahara's (1968) four numerical experiments, but with a bell-shaped obstacle instead of a ridge, Oobayashi (1970) suggested that the curve *FAB* shown in figure 2 separates the steady from non-steady regimes in the three-dimensional case as well. A more thorough and systematic examination of this question is attempted here.

The present numerical experiments investigate the dependence of the critical curve separating the region of non-steady from steady flow on the cross-stream obstacle width. As the interest here is with atmospheric applications, the experiments concentrate on the parameter range $F_0 < 1$. The results of these experiments are presented in §2, and quantitative measures to represent the magnitude of flow over versus flow around for steady flows are suggested.

Laboratory experiments were conducted in the Environmental Protection Agency Fluid Modeling Facility flow tank to corroborate and extend the results of the numerical model. The flow-tank experiments investigated the flow of two homogeneous hydrostatic superposed layers of fluid past an isolated obstacle, as shown in figure 1 (the diagram must be inverted to correspond to the flow-tank configuration). The analysis of the two-dimensional steady case for two finite-depth layers has been presented by Long (1972) and reviewed by Baines & Davies (1980). Additional parameters must be defined: $r = h_0/(h_0+h_1)$ and $g' = g(\rho_0-\rho_1)/\rho_0$. The modification of the critical curve *FAB* in figure 2 by the presence of the finite-depth upper layer is presented in figure 3, taken from Baines & Davies (1980), where F_0 is the initial

Froude number of the lower layer. As $r \to 0$ the single-layer solution to (1) is approached, with g' replacing g. For $r < 0.5$ and $F_0 < 1.0$ the qualitative description of the regimes on either side of the appropriate critical curve of figure 3 is essentially unchanged.

The flow-tank experiments that extend this analysis to the case of a three-dimensional obstacle are presented in §3. The experiments correspond to values of $r = 0.125$, 0.25, 0.37, and $h^* = 0.667$, 1.0, 2.0. These r-values are small enough that for simplicity only the $r = 0$ curve will be presented with the plotted results, with little loss of accuracy.

The equation for the line BC in figure 2 is, from Houghton & Kasahara (1968),

$$F_0 = \frac{h^* - 1}{h^*}\left[h^* \frac{1 + h^*}{2}\right]^{\frac{1}{2}}. \tag{9}$$

The region below this curve, with $h^* \geqslant 1.0$ and small F_0 corresponds, in the two-dimensional case, to complete blocking. With a three-dimensional obstacle, the flow can go around, and the criterion (9) is no longer appropriate. A steady solution may exist with the velocity vanishing only on the centreline $y = 0$, where the interface impinges on the obstacle. If the interface impinges just at the crest of the hill, then (2a) gives

$$h_0 + \frac{u_0^2}{2g'} = h_{\mathrm{m}};$$

that is, a tentative criterion for impingement could be taken as

$$F_0^2 < 2(h^* - 1). \tag{10}$$

Curves from (9) and (10) will be plotted for comparison with data from the laboratory experiments in §3.

2. The numerical experiments

2.1. *Formulation and testing*

The arrangement of variables shown in figure 4 has been shown to give the most accurate phase speed for linear gravity waves (Arakawa & Lamb 1977) and will be used in the present model. Conservation of momentum and energy are of primary importance in the present problem, making it desirable to use a scheme that maintains finite-difference analogues of the equations for the conservation of total energy and u-momentum. If the most natural form is chosen for the finite-difference analogue of (1c), then the simplest such scheme for (1a, b) of second-order accuracy that can be derived for the chosen grid is given as follows, with the time derivative left in continuous form at this point:

$$\frac{\partial}{\partial t}(h^u u)_{i,j+\frac{1}{2}} = -\frac{1}{d}[(F^u \bar{u}^x)_{i+\frac{1}{2},j+\frac{1}{2}} - (F^u \bar{u}^x)_{i-\frac{1}{2},j+\frac{1}{2}} + (G^u \bar{u}^y)_{i,j+1} - (G^u \bar{u}^y)_{i,j}] - (h^u \delta_x \Phi)_{i,j+\frac{1}{2}}, \tag{11a}$$

$$\frac{\partial}{\partial t}(h^v v)_{i+\frac{1}{2},j} = -\frac{1}{d}[(F^v \bar{v}^x)_{i+1,j} - (F^v \bar{v}^x)_{i,j} + (G^v \bar{v}^y)_{i+\frac{1}{2},j+\frac{1}{2}} - (G^v \bar{v}^y)_{i+\frac{1}{2},j-\frac{1}{2}}] - (h^v \delta_y \Phi)_{i+\frac{1}{2},j}, \tag{11b}$$

$$\frac{\partial}{\partial t} h_{i+\frac{1}{2},j+\frac{1}{2}} = -[\delta_x(h^u u) + \delta_y(h^v v)]_{i+\frac{1}{2},j+\frac{1}{2}}, \tag{11c}$$

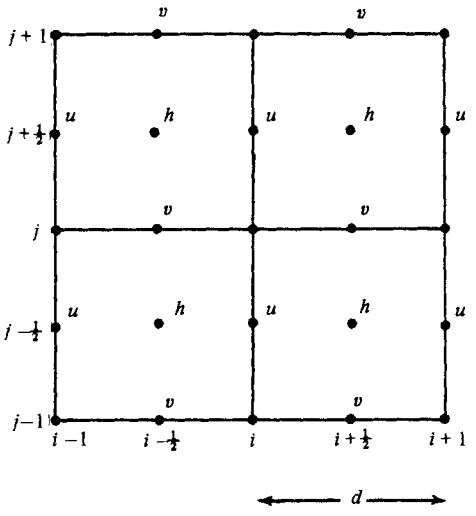

FIGURE 4. Staggered grid used in the numerical model.

where

$$\Phi_{i,j} \equiv (h+h_s)_{i,j},$$

$$h^u_{i,j} \equiv \bar{h}^x_{i,j}, \quad h^v_{i,j} \equiv \bar{h}^y_{i,j},$$

$$\bar{\xi}^x_{i,j} \equiv \tfrac{1}{2}(\xi_{i+\frac{1}{2},j}+\xi_{i-\frac{1}{2},j}), \quad \bar{\xi}^y \equiv \tfrac{1}{2}(\xi_{i,j+\frac{1}{2}}+\xi_{i,j-\frac{1}{2}}),$$

$$F^u_{i,j} \equiv \overline{(h^u u)}^x_{i,j}, \quad G^u_{i,j} \equiv \overline{(h^u u)}^y_{i,j},$$

$$F^v_{i,j} \equiv \overline{(h^v v)}^x_{i,j}, \quad G^v_{i,j} \equiv \overline{(h^v v)}^y_{i,j},$$

$$(\delta_x \xi)_{i,j} \equiv \frac{1}{d}(\xi_{i+\frac{1}{2},j}-\xi_{i-\frac{1}{2},j}), \quad (\delta_y \xi)_{i,j} \equiv \frac{1}{d}(\xi_{i,j+\frac{1}{2}}-\xi_{i,j-\frac{1}{2}}).$$

(With this scheme u-momentum is nearly conserved throughout the experiments, although there is a formal guarantee only for the case of no topography.)

Leapfrog time differencing was used – a second-order-accurate scheme that is conditionally stable and neutral when applied to the linearized gravity-wave equation with advection:

$$\xi^{n+1}-\xi^{n-1} = 2\Delta t f^n(u,v,h). \tag{12}$$

A forward step was inserted periodically to suppress the weak instability that arises with the use of a three-level scheme in nonlinear equations (Lilly 1965). It was necessary to use a Δt that easily satisfied the criterion for linear computational stability for a two-dimensional grid

$$\sqrt{2}\,(u_0+(gh_0)^{\frac{1}{2}})\frac{\Delta t}{\Delta x} \leqslant 1. \tag{13}$$

With a neutral time-differencing scheme, solutions with discontinuities cannot be maintained for long times, as they continue to steepen until the integration fails. In a real fluid, a jump is associated with energy loss through turbulent mixing, and can be maintained with a finite amplitude (Long 1954). The use of a dissipative scheme would damp the numerical oscillations near a jump, but could also influence the jump formation and thus obscure a main point of investigation.

The difference scheme was tested for the case of a y-independent wave progressing

down a flat-bottomed channel into still fluid. The time and position at which the wave will steepen and approach a breaking point can be calculated from (1) and depend on amplitude, frequency and equilibrium water depth (Stoker 1957, p. 356). For a wide range of parameters, the model predicted the correct position and time with good accuracy.

All of the obstacle shapes considered had a triangular cross-section in the (x, z)-plane, with base half-length l_x. A smoother shape with no discontinuity of slope would tend to minimize separation effects in a real fluid, and thus make the comparison between results of laboratory experiments and those of an inviscid numerical model more valid, especially in the lee. However, to study the dependence of the flow on the obstacle shape and size, it was advantageous to characterize the geometry in the fewest number of parameters. The linear slope has an additional advantage in that no truncation error arises in the finite-differencing from the pressure-gradient term Δh_s.

For the numerical experiments, three obstacle base half-widths l_y were considered. The ridge was used for comparison with analytical solutions as well as previous numerical studies. The cone, with $l_y = l_x$, corresponded to the obstacle used in the laboratory flow tank. The truncated ridge, a cone sliced in half through the centre with a ridge inserted between the halves, was included to clarify the transition between two-and three-dimensional flows.

The channel extended in x from $-L_x$ to $+L_x$, where a cyclic boundary condition was assumed. The channel was made long enough so that, during the time period of interest, the motion was steady near the obstacle before the downstream field could affect the upstream motion. Sidewalls were assumed at the lateral boundaries $y = \pm L_y$.

For the cases with three-dimensional topography it was desired to choose the channel width large enough that the side boundary conditions did not significantly affect the flow in the vicinity of the obstacle. By repeating many experiments, varying only the width of the channel, it was found that with $L_y/l_y \geqslant 2$ the velocities at $(0, l_y)$ differed by only a few percent.

To facilitate comparison with the laboratory experiments, relative channel and obstacle dimensions were fixed so as to correspond to those of the flow tank to be discussed in §3. For a gridlength $\Delta x = \Delta y = \Delta s$, the cone was of radius $5\Delta s$ and the truncated ridge of half-widths $l_x = 5\Delta s$, $l_y = 9\Delta s$. The channel was of length $250\Delta s$, depth $2.5\Delta s$ and cross-sectional half-width $12\Delta s$ for the cone and $22\Delta s$ for the truncated ridge. Thus the ratio $h_0/2l_x$ relevant to the validity of the hydrostatic approximation was 0.25 in both laboratory and numerical experiments.

To fix the gridlength, a set of experiments was repeated varying only the resolution, with from 5–40 points defining the conical obstacle. The results differed only in the amplitude of small-scale noise generated near the obstacle. The chosen spacing, with averaging of the final fields over 25 time steps, produced results as smooth as the finest resolution with no change in the critical values.

The initial conditions were an undisturbed free surface of height h_0 and a constant zonal velocity u_0. For a specified topography, (11) and (12) were integrated in time until the solution in the vicinity of the obstacle became steady or a jump formed, indicating that the solution was in the nonsteady region of figure 2. The regime of the asymptotic state was determined by the following criteria:

(*a*) subcritical if F increases with increasing x to a maximum value less than one at the crest, then decreases in the lee;

(*b*) a jump regime if F increases over the crest, passes through a value close to one at the crest to a relative maximum in the lee, and then jumps to the initial F_0 value.

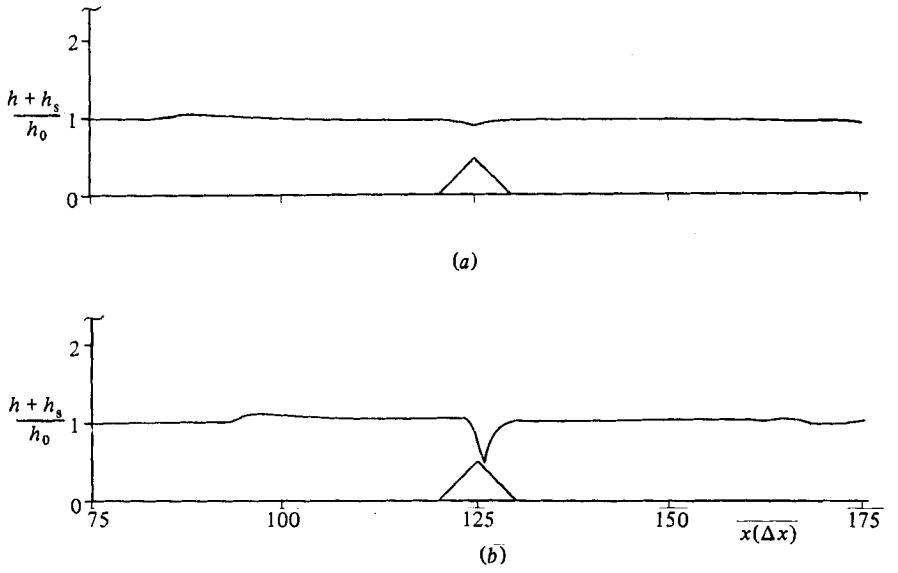

FIGURE 5. Normalized surface height for ridge case with $h^* = 0.5$: (a) $F_0 = 0.2$; (b) $F_0 = 0.3$.

Test experiments similar to those of Houghton & Kasahara (1968) were performed: two time integrations of the model using the ridge obstacle, with an obstacle height $h^* = 0.5$ and $F_0 = 0.2, 0.3$, which should be in different regimes according to figure 2. The normalized surface heights $(h+h_s)/h_0$ shown in figures 5(*a*, *b*) correspond to 3.0 s or 600 time steps for the $F_0 = 0.2$ case and 2.4 s for the $F_0 = 0.3$ case (fields here and in all figures from numerical experiments are averaged over the final 25 time steps to smooth small-scale noise). Comparison with the analytically proposed solutions of figure 2 shows that the predicted features in these two-dimensional cases are well represented.

2.2. *Results*

An experimental curve analogous to *FAB* in figure 2 was constructed for the case of the ridge obstacle, i.e. repeated time integrations were carried out to locate approximate values of h^* and F_0 on the critical curve. Experiments were conducted for ridge heights $h^* = 0.2$, 0.5 and 0.8. The approximate critical curve is shown (dashed) in figure 6, with the lower branch of *FAB* from figure 2 given (solid) for comparison. The difference between the two curves is very small and can be attributed to the truncation error incurred by the use of finite-difference approximations.

A second set of experiments was then performed for the case of the truncated ridge, in which the flow is no longer two-dimensional. As an example, figures 7(*a–c*) show the steady flow pattern for the case $h^* = 0.5$, $F_0 = 0.3$, at $t = 3.0$ s. Figure 7(*a*) shows streamlines of the flow field and figures 7(*b*, *c*) present contour maps of the non-dimensional surface-height perturbation and local Froude number respectively. The flow is just critical at the obstacle crest along the $y = 0$ line, while the flow around the sides of the obstacle remains subcritical.

Experiments with the truncated ridge for $h^* = 0.2, 0.5, 0.8$ were used to determine the transition curve shown dash–dotted in figure 6. The transition line from subcritical flow to flow with a jump in the lee has clearly shifted; for a given flow speed a higher obstacle is required to produce a jump along the centreline.

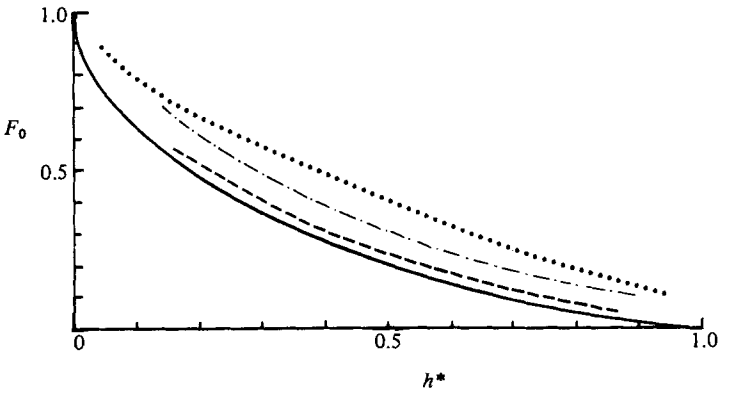

FIGURE 6. The critical curves as determined by numerical experiments for (*a*) ridge (dashed); (*b*) truncated ridge (dash–dotted); (*c*) conical obstacle (dotted); (*d*) analytical curve from (5) (solid).

The largest set of experiments was performed for the case of a conical obstacle; the (F_0, h^*) pairs examined are indicated in figure 8(*c*). The effect of increased three-dimensionality is seen in the steady flow results for the case $h^* = 0.5$, $F_0 = 0.3$ at $t = 3.0$ s shown in figures 8(*a*, *b*); the flow regime in this case is subcritical everywhere. The experimentally determined transition line is shown (dotted) in figure 6.

The streamline maps of figures 7(*a*), 8(*a*) and the shifted transition line of figure 6 provide qualitative evidence of the deviation of the flow around a three-dimensional obstacle, but a quantitative measure is still lacking. Two different measures are proposed here and applied to the data from the experiments with the conical obstacle. For the present case of homogeneous nonrotating fluid the magnitude of variation of flow around is not large, but the usefulness of the proposed measures can be tentatively evaluated.

The first measure utilizes the mass flux hu, which for the two-dimensional steady case is constant in x and equal to the initial upstream value $h_0 u_0$. With y-dependence, the divergence of meridional mass flux, $\partial hv/\partial y$, can change this value. The profile in y through the centre of the conical obstacle (along the $x = 0$ line) of $hu/h_0 u_0$ for the sample case $h^* = 0.5$, $F_0 = 0.3$ is shown in figure 9(*a*). Note that there is little deviation from the undisturbed value at the edges of the channel. A single number can be extracted from each such curve by considering the normalized integral of values over the obstacle:

$$m_1 = 1 - \frac{1}{h_0 u_0} \frac{1}{l_y} \int_0^{l_y} hu(0, y)\, \mathrm{d}y.$$

Values of this measure range between 0, for the case with all flow over the obstacle, and 1, for all flow around. A value of m_1 was calculated from the asymptotic flow pattern of each integration classified as a subcritical case. Figure 9(*b*) shows contours of the measure m_1; the values increase most rapidly with increasing h^*.

A second measure of the dependence of flow around on h^* and F_0 is derived by graphical determination of the velocity tangent line just touching the obstacle. The distance d of the upstream position of this streamline from the $y = 0$ line (see figure 10*a*) can be taken as a measure of the flow deflection. When normalized by the obstacle half-width l_y, the measure

$$m_2 = 1 - \frac{d}{l_y}$$

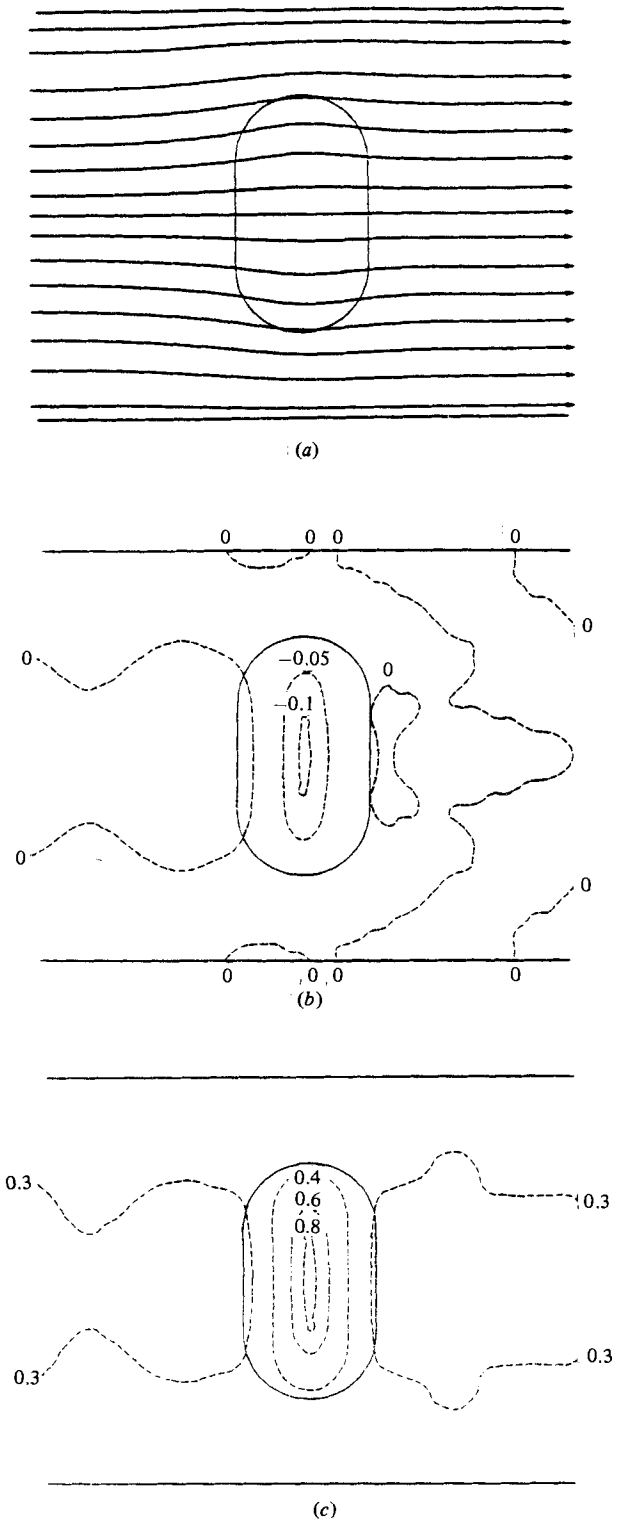

FIGURE 7. Steady flow for the truncated ridge with $h^* = 0.5$, $F_0 = 0.30$: (*a*) streamline map; (*b*) surface-height perturbation contours; (*c*) contours of local Froude number.

takes values between 0, when there is no deflection, and 1, in the limiting case that the flow on the centreline just passes around the obstacle. Contours of m_2 for the experiments with the conical obstacle in the subcritical region are presented in figure 10(*b*); the values increase with increasing F_0 and h^*.

3. The laboratory experiments

3.1. *Apparatus and techniques*

All of the experiments were performed in the large towing tank of the U.S. Environmental Protection Agency Fluid Modeling Facility. The towing tank and associated equipment is described in detail in Hunt & Snyder (1980). The towing tank is 1.2 m deep, 2.4 m wide and 25 m long, has an aluminium framework and is lined with acrylic plastic. The tank may be filled with an arbitrary stable density stratification using salt water (specific gravity 1.0–1.2). A towing carriage may be pulled along the tank at uniform speeds of 5–50 cm s^{-1}.

For the present experiments sufficient fresh water or salt water of low specific gravity was fed into the channel to give the desired upper-layer depth h_0 (see figure 1, inverted). A lower layer h_1 of greater specific gravity was then slowly introduced from the bottom of the tank. The entire filling operation requires about 66 m^3 of water and takes approximately 4 h.

Density profiles were obtained by drawing samples over the depth of the tank at one or two centimetre intervals. The specific gravity of the sample was determined with an electronic balance (Mettler balance PS 200). The estimated error in the specific-gravity determination was 0.0005 random and +0.0005 systematic. Two different density ratios were used to obtain a wide range of the independent variables. The nominal density differences were $(\rho_1-\rho_0)/\rho_0 = 0.02$ and 0.20.

Mechanical mixing during filling and molecular diffusion during filling and operation resulted in a minimum obtainable interface thickness of about 3 cm. After the day's experiments the interface thickness often increased to 5–6 cm. The sharper interface was reestablished overnight by selective withdrawal of the fluid near the interface, at approximately 0.2–0.4 m^3/h, and replacement by denser fluid at the bottom and lighter fluid at the top at the appropriate rates. A change in interface position was obtained by introducing denser fluid at the bottom of the tank and skimming lighter fluid from the top.

The model hill was conical in shape, vacuum moulded from 6 mm acrylic plastic. The hill was mounted in a base plate of acrylic plastic attached to a framework of rectangular aluminium tubing. The base plate was immersed approximately 0.5 cm into the water and the hill towed upside down. The aluminium tubing supporting the baseplate was suspended from the towing carriage through four jackscrews, which permitted levelling of the baseplate. The baseplate had a 45° bevelled upstream edge.

The height h_m of the top of the conical hill from the baseplate was 23.4 cm, the included angle of the cone was 127°, and the distance $2l_x$ across the base of the hill was 93.6 cm. The total depth H of the two layers was fixed at 108 cm. The height of the interface from the obstacle base was then varied such that for the sets of experiments reported here $h^* \equiv h_m/h_0 = 0.67, 1.0, 2.0$.

The experimental results obtained in this study were documented by several means of flow visualization. Shadowgraphs were obtained on a translucent plexiglass sheet on the side of the towing tank. Another method of flow visualization was that of photographing the plumes resulting from point sources of dye released from various

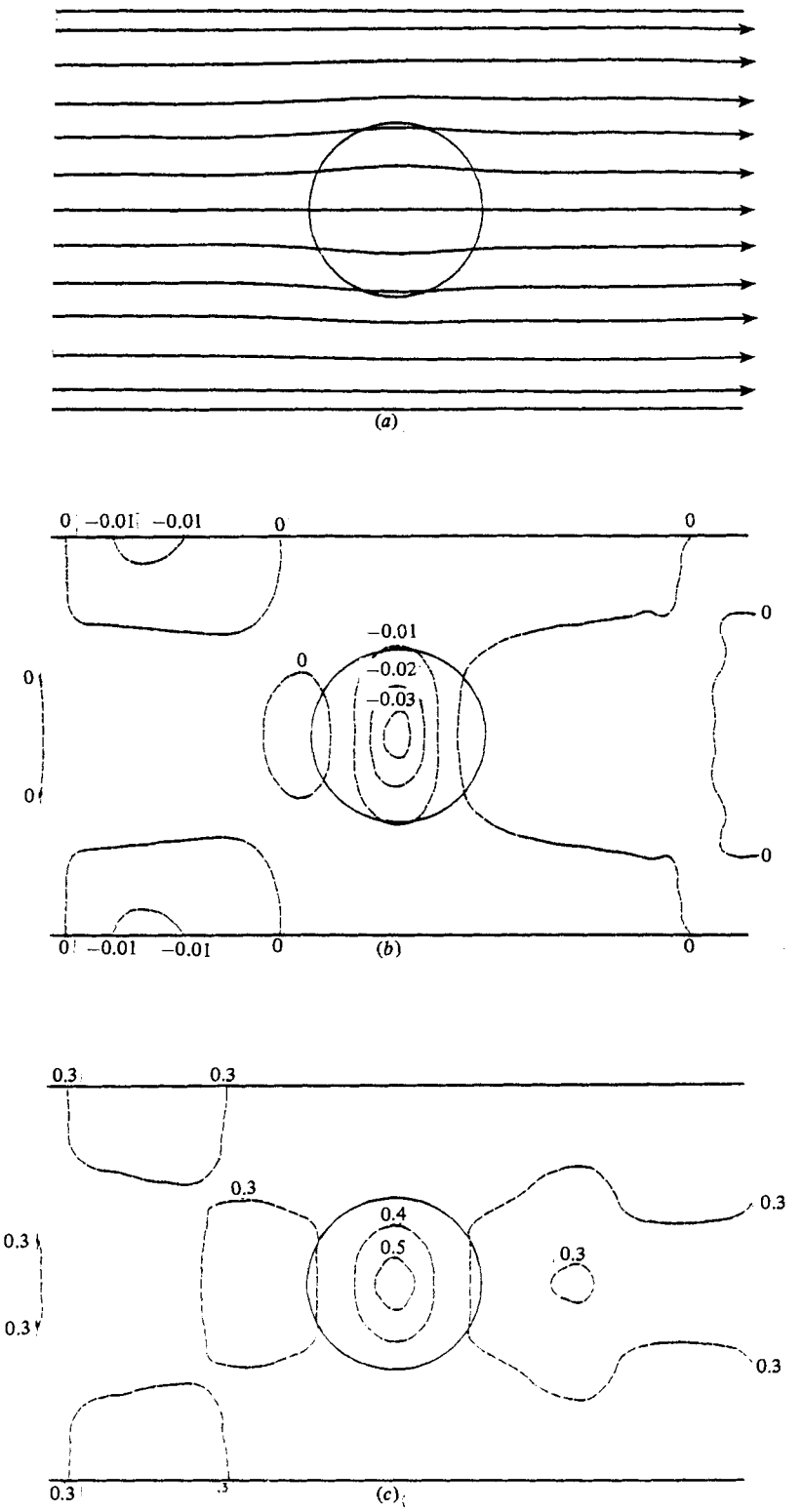

FIGURE 8(*a–c*). For caption see facing page.

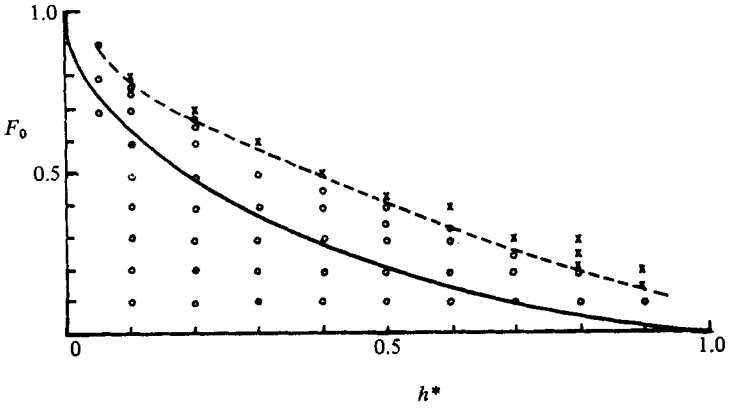

(*d*)

FIGURE 8. Steady flow for the conical obstacle with $h^* = 0.5$, $F_0 = 0.30$: (*a*) streamline map; (*b*) surface-height perturbation contours; (*c*) contours of local Froude number; (*d*) experiments to define critical curve (○, subcritical; ×, non-steady).

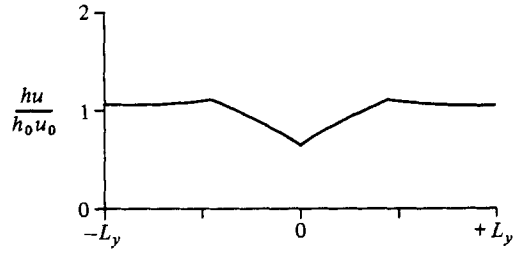

(*a*)

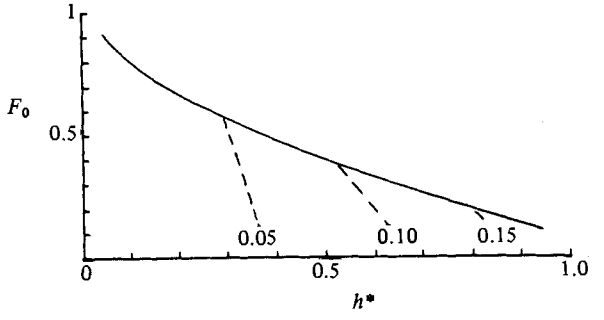

(*b*)

FIGURE 9. (*a*) Plot of normalized momentum flux hu/h_0u_0 as a function of y along $x = 0$ for the case of the conical obstacle, $h^* = 0.5$, $F_0 = 0.30$. (*b*) Contours of m_1 for conical-obstacle experiments with flow in subcritical region.

upstream positions. Care was taken to ensure that the dye, Warner Jenkinson no. 393 blue food dye, was released at the specific gravity of the ambient fluid. Releases at local fluid velocity (isokinetic) were attempted, although this was not essential for the visualization studies. Side and top views were obtained with a 35 mm camera. Experiments were made with vertical and horizontal rakes of sources of internal diameter either 0.8 mm or 1.6 mm. The vertical rake had 11 sources at 2 cm spacing,

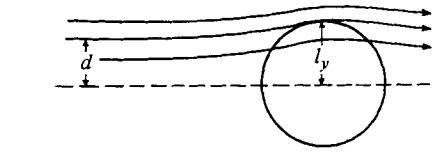

(a)

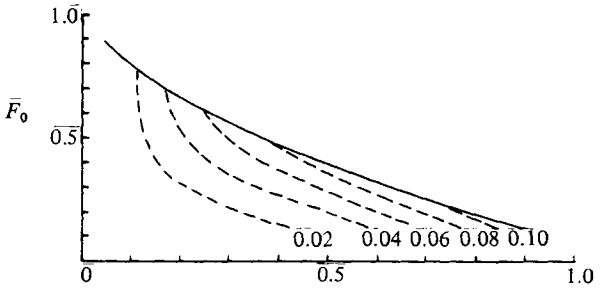

(b)

FIGURE 10. (a) Diagram showing definition of the length d used in m_2. (b) Contours of m_2 for conical obstacle experiments with flow in subcritical region.

with the source nearest the base being 2 cm off the base. Two horizontal rakes were used, each with 5 sources. The first of these rakes had sources located at $y = -5.5$ cm, 0, +5.5 cm, +11 cm, and +16.5 cm, where $y = 0$ is directly upstream of the centre of the hill. The other rake had sources located at $y = -5.5$ cm, 0, 11.5 cm, 25 cm and 45 cm. The technique used is considered in more detail in Hunt & Snyder (1980). In some experiments dye was placed at the interface to indicate the interface movement more clearly.

In most of the sets of experiments a density difference of $\Delta\rho/\rho \approx 0.02$ was used. In the few sets for which $\Delta\rho/\rho \approx 0.2$, the larger density difference led to difficulties in interpreting and recording the flow-visualization studies, for example causing unusual refractive effects in some of the side-view photographs. When these experiments were rerun to obtain shadowgraphs, a density difference $\Delta\rho/\rho$ of approximately 0.02 was used and the results were in all cases in good agreement with the earlier experiments.

3.2. *Results*

An initial set of experiments was performed for $h^* = 0.67$ to check the validity of the shallow-water assumption that an initially vertical column of fluid remains vertical ($\partial \boldsymbol{v}_H/\partial z = 0$). Estimates of the change of flow direction in the vertical were made by releasing dye from a vertical rake with eleven sources, offset from the centreline by 15.5 cm. Such experiments were conducted for the range of Froude numbers to be examined in the present study, and for all cases the plumes had a very limited lateral spread as shown, for example, in figure 11 for $h^* = 0.67$ and $F_0 = 0.41$. Estimation of change of velocity magnitude with height is not documented here, for discrepancies in the rate and time of initial dye release made it difficult to judge the shear of the flow. Another attempt utilized a discontinuous release, but the results were difficult to quantify. However, the observations did not contradict the assump-

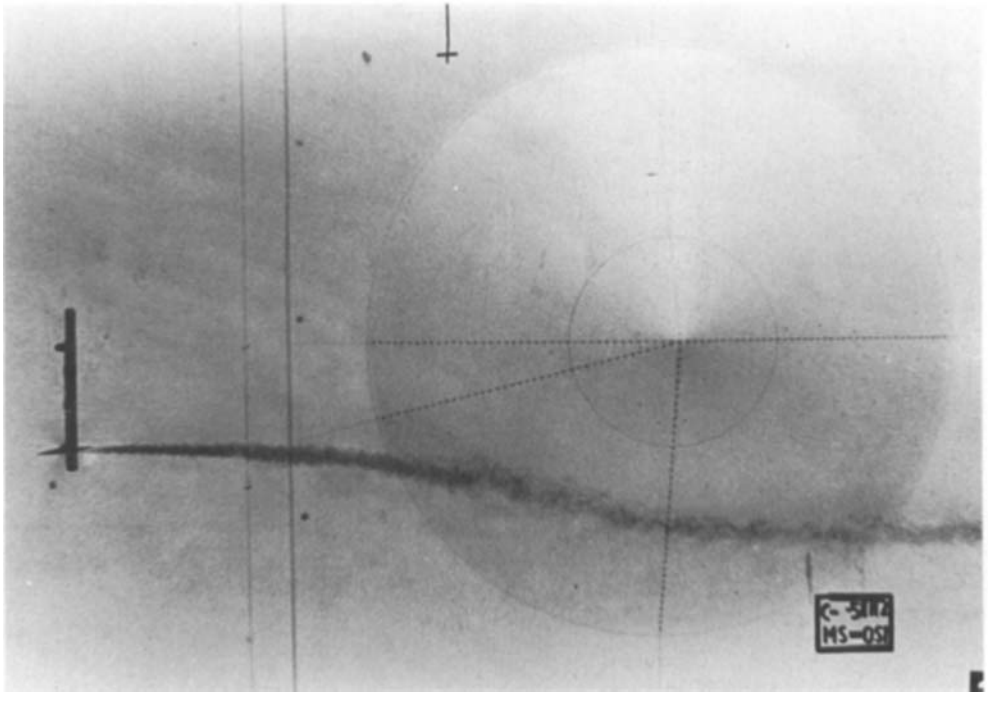

FIGURE 11. Top-view photograph showing lack of plume spread; $h^* = 0.67$, $F_0 = 0.41$.

tion of an essentially uniform velocity in the vertical outside a surface boundary layer of a few centimetres.

Another point to be discussed before comparisons between laboratory fluid flow and the results of the numerical model can be made is that of flow separation. At the Reynolds numbers used in this study, $1.5 \times 10^4 \leqslant u_0 h_m/\nu \leqslant 1.0 \times 10^5$, and with the conical obstacle, it was anticipated and observed that the flow would, in general, separate from the surface of the hill, giving rise to a region of recirculating flow in the lee. Further downstream there is usually found a region of decreased mean velocity and increased velocity fluctuations – the turbulent wake. The perturbations decrease in strength with increasing distance from the obstacle, while the dimensions of the wake grow. The nature and geometry of the flow separation and wake are of some consequence for air-pollution studies; however, they are of interest here only insofar as they may affect the approach flow and nature of the regime over the obstacle. It will be shown that for cases with similar h^* and F_0 the flow pattern upstream and over the obstacle produced in the laboratory fluid corresponds to that predicted by the inviscid numerical model.

The F_0 and h^* values investigated through laboratory experiments are indicated in figure 12. The figure characterizes the flow regime by interface shape for the three sets of laboratory experiments ($h^* = 0.67$, 1.0, 2.0). Those cases for which the interface either remained horizontal or had a slight depression over the crest are indicated by open circles. The cases in which the interface swelled over the crest are shown as small squares. The cases where strong downslope flow was observed in the lee are indicated with crosses. In these cases the flow rises to its downstream level through a hydraulic jump or through an undular jump. Those cases where the interface impinges on the hill rather than rises over the crest are shown as closed circles.

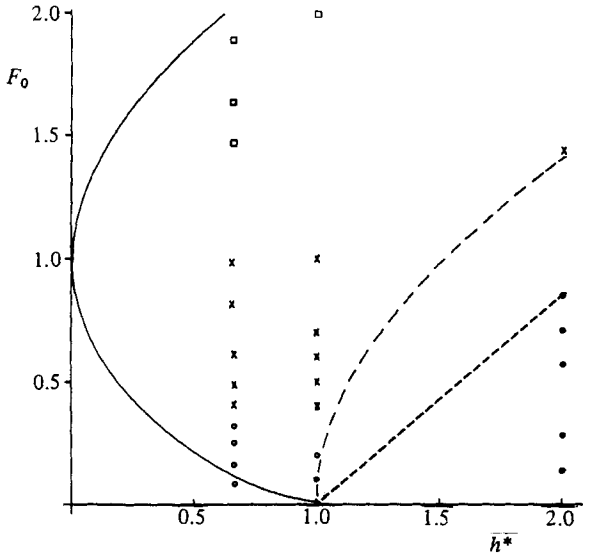

FIGURE 12. Classification of laboratory experiments into flow regimes: ○, interface is horizontal and depressed at crest; ●, interface impinges on obstacle; □, interface rises over crest; ×, strong downslope flow in the lee; ---, (9); ——, (10).

The cases with $h^* = 0.67$ and $F_0 \leqslant 0.6$, two shadowgraphs of which are shown as figure 13, tend to corroborate the results of the numerical model as to the shift of transition curve and effect of Froude number on the flow regime. For $F_0 \leqslant 0.33$ (see figure 13*a*) the interface is nearly horizontal, although there is a slight depression and recovery of the interface near the crest at the channel centre. The mixing at the interface is probably a result of the flow separation and small instabilities on the interface. For $F_0 \approx 0.4$–0.6 (see figure 13*b*) the interface at the channel centre was bent down parallel to the lee face of the hill for about half the length of that face before rising to overshoot its equilibrium position. This resulted in separation being inhibited at the crest, occurring well down the back of the hill. The lee jumps observed in the flow tank experiments are less steep than those in the numerical experiments, for those in the laboratory fluid are dissipated by turbulence and mixing. At Froude numbers $F_0 \geqslant 0.33$ there are waves on the interface in the lee of the hill. The waves have a maximum amplitude of approximately 25 cm and a wavelength that increases with Froude number, from about 0.67 m at $F_0 = 0.33$, 1.5 m at $F_0 = 0.49$ to approximately 4 m at $F_0 = 0.61$. For $F_0 > 1.0$ the interface rises slightly over the crest and then descends to its original level in the lee. The flow separation again occurs at the crest but the vertical wake growth is decreased to become more nearly horizontal (at least close to the hill).

Streamline patterns were obtained for comparison with those from the numerical model using the horizontal rake described in §3.1. The rake was set at half the hill height (11.7 cm) and vertical photographs taken. The plume paths for $F_0 = 0.16$ are shown in figure 14; the plume paths for $F_0 = 0.33$ were not significantly different, and figure 14 may be compared with the numerical-model result in figure 8(*a*). While the two streamline patterns are similar, there is more deflection of the streamlines in the laboratory study. The measure m_2 was estimated at 0.18 for $F_0 = 0.16$ and 0.33, whereas the numerical results (figure 10*b*) suggest values of 0.06 and 0.10 respectively. The large value of m_2 for the laboratory experiments is undoubtedly a result of flow separation and consequently larger effective obstacle size.

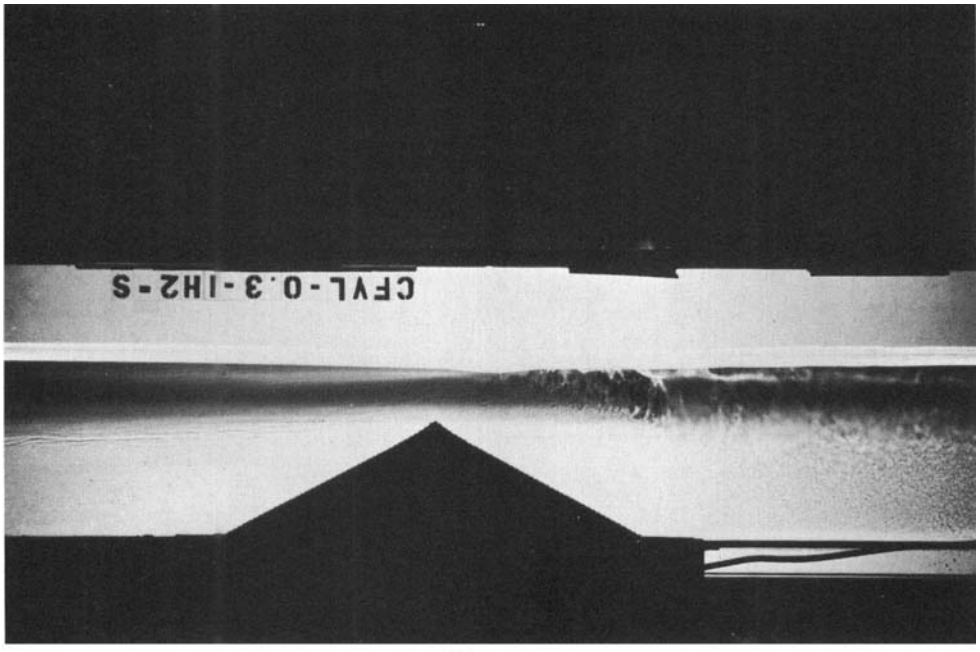

(*a*)

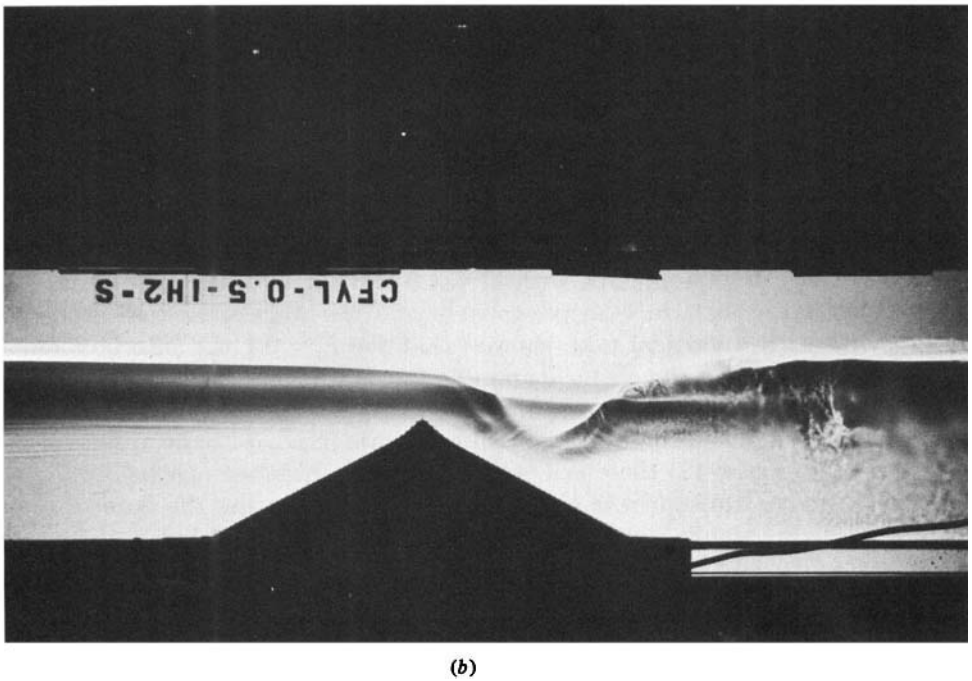

(*b*)

FIGURE 13. Shadowgraphs for the case $h^* = 0.67$: (*a*) $F_0 = 0.25$; (*b*) $F_0 = 0.41$.

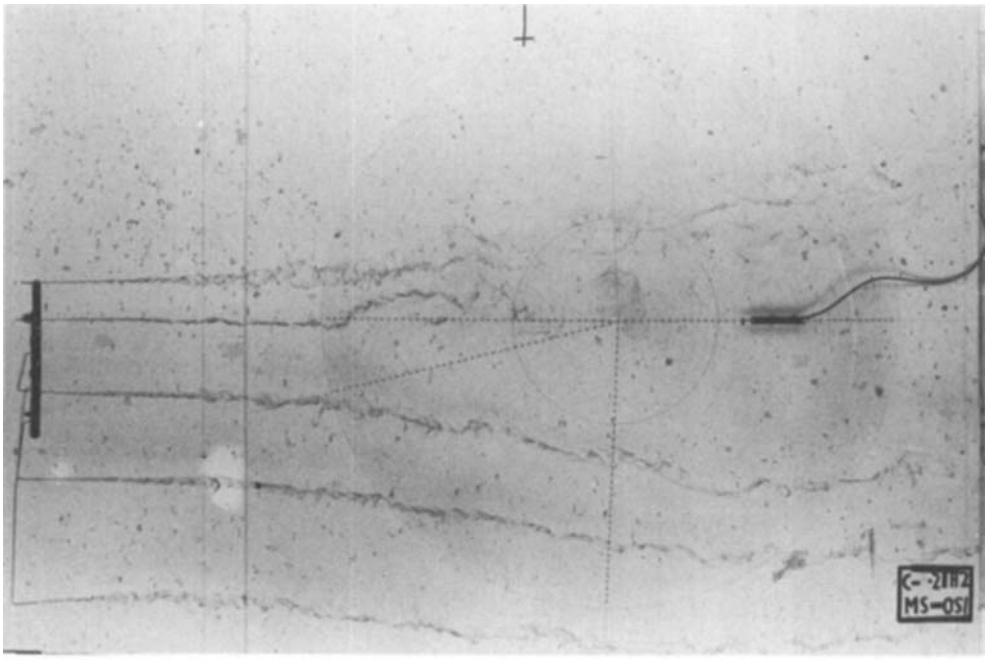

FIGURE 14. Plume-trajectory photographs, top view; $h^* = 0.67$, $F_0 = 0.16$.

An attempt was made to obtain estimates of the mass flux hu at the obstacle crest for comparison with results used in calculating m_1 for the numerical model. Estimates of the depth h_c of the flow above the crest of the hill were made by visual observation; estimates of the velocity u_c of the flow there were made with a small propeller anemometer mounted with the propeller centre set two centimetres above the hill crest. The resulting estimates of $h_c u_c / h_0 u_0$ are plotted against F_0 with those from the numerical model in figure 15. The differences between the numerical and experimentally derived data can perhaps be explained through the presence of separation in the laboratory experiments.

The second set of experiments, with $h^* = 1.0$ and the undisturbed interface level with the crest of the obstacle, is an extension beyond the range of the numerical model. Experiments with a vertical rake showed that for $F_0 = 0.1$ the interface remains horizontal, impinges on the obstacle and all plumes separate to go around the crest (see figure 16). At $F_0 = 0.4$ the interface just clears the crest and is drawn down in the lee in a weak hydraulic jump. Lower plumes again impinge on the upstream slope. At $F_0 = 0.5$ (see figure 17) there is a small rise in the interface just before the crest and then a strong drawdown in the lee, the interface nearing the base of the hill before a strong hydraulic jump. The plumes all clear the crest, but note how close all the plumes come to the lee surface of the hill. There are no large-amplitude waves in the lee. With Froude numbers of 0.6 and 0.7, there is a distinct drawdown of the interface at and beyond the crest, nearly reaching the hill base. The interface then rises back to the level of the undisturbed interface with no obvious jump but with strong wave motion in the lee. A long wave of elevation travels upstream. At $F_0 = 1.0$ there is no obvious upstream influence except that the interface rises slightly just ahead of the crest of the hill before descending in the lee. The descent in the lee is not as close to the lee face as for $F_0 = 0.6$ and 0.7. There are still waves in the far

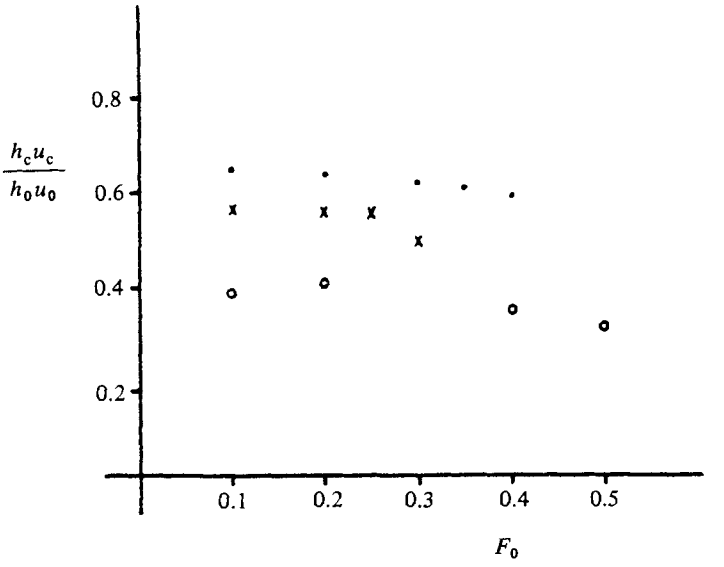

FIGURE 15. Comparison of normalized mass flux at crest of obstacle: laboratory data with $h^* = 0.67$ (○); numerical-model data with $h^* = 0.6$ (●) and $h^* = 0.7$ (×).

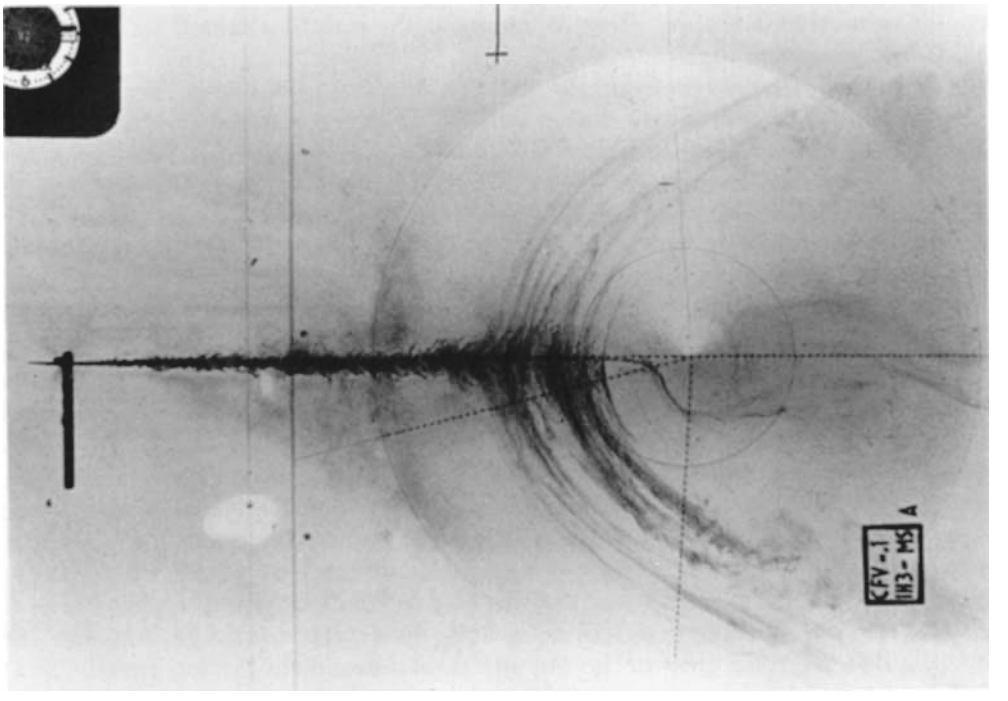

FIGURE 16. Top-view photograph of vertical-rake plume release for the case $h^* = 1.0$, $F_0 = 0.1$.

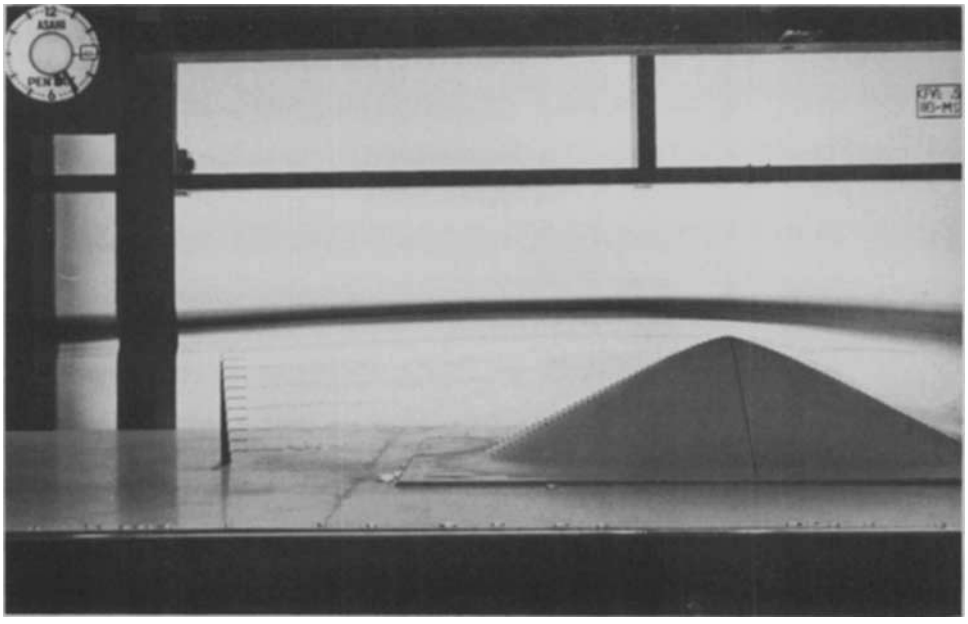

FIGURE 17. Side-view photograph of vertical-rake plume release for the case $h^* = 1.0$, $F_0 = 0.5$.

lee of the hill. At $F_0 = 2.0$ the interface rises symmetrically over the obstacle with little wave motion in the lee. There is mixing at the interface caused by the velocity field in the separated region.

In figure 12 the curve from (9) defining the 'total-blocking' regime in the two-dimensional case is shown dotted and the proposed criterion (10) for interface impingement is shown dashed. For the experiments with $h^* = 2.0$ no lower-layer flow passes over the crest for the lower Froude numbers, as expected from (10). For $F_0 = 0.14$ the interface is little disturbed upstream or downstream as it passes around the hill. With $F_0 = 0.28$ the interface rises slightly as the flow stagnates on the upstream face of the hill, and then descends below its upstream level as it passes around the side of the hill. There is turbulence and mixing in the lee of the hill, with the interface returning to near its upstream level. Such flow is important for air-pollution studies, as a pollutant may be advected onto the hill side rather than diffuse to it, allowing surface concentrations nearly equal to the maximum concentration in the plume. For further discussion of this point see Snyder, Britter & Hunt (1979). At Froude numbers of 0.57–0.85, a long wave of elevation travels upstream ahead of the hill. As the Froude number increases there is also a more distinct rise of the interface as the flow stagnates, and an associated lowering of the interface near the hill as the flow travels around the side of the obstacle. The turbulence and mixing in the near lee give way to small-amplitude waves in the far lee. At a Froude number of 1.4 there is little discernible upstream influence. The interface rises over the crest of the hill and then descends in the lee, parallel to the lee face, to nearly reach the base. There is no separation on the lee face of the hill, and the interface rises slowly in the far lee to its upstream level. At a Froude number of 2.8 (not shown on graph) the interface rises symmetrically over the obstacle to clear the crest and then returns to its upstream level in the lee. Thus (10) is in agreement with the limited data available.

Experiments for the case $h^* = 2.0$ with the vertical rake located on the $y = 0$ line

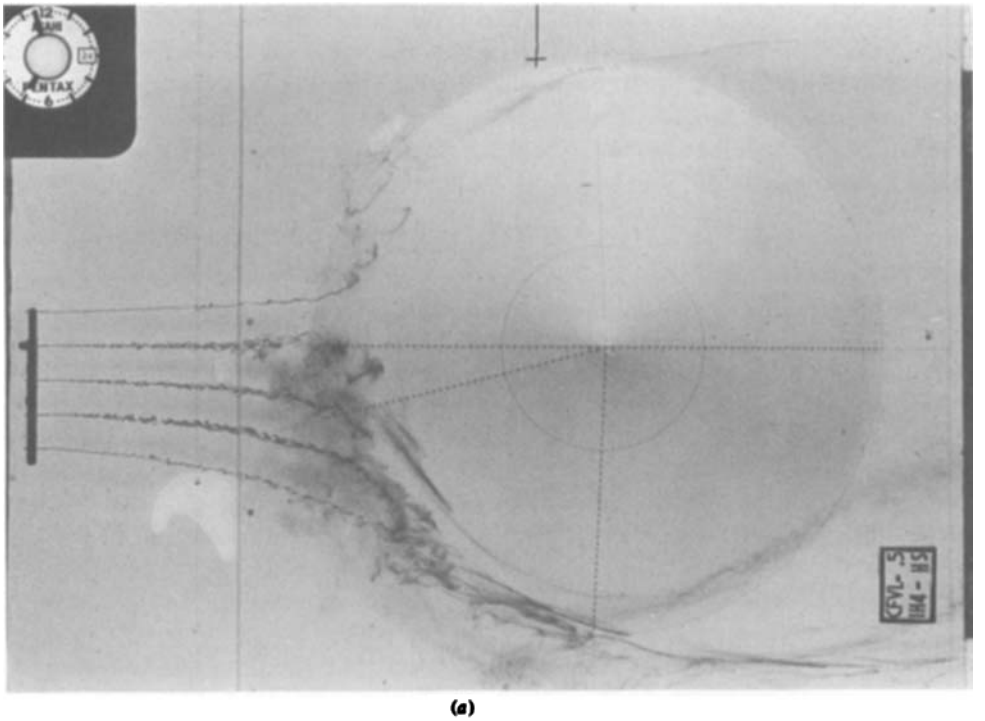

(*a*)

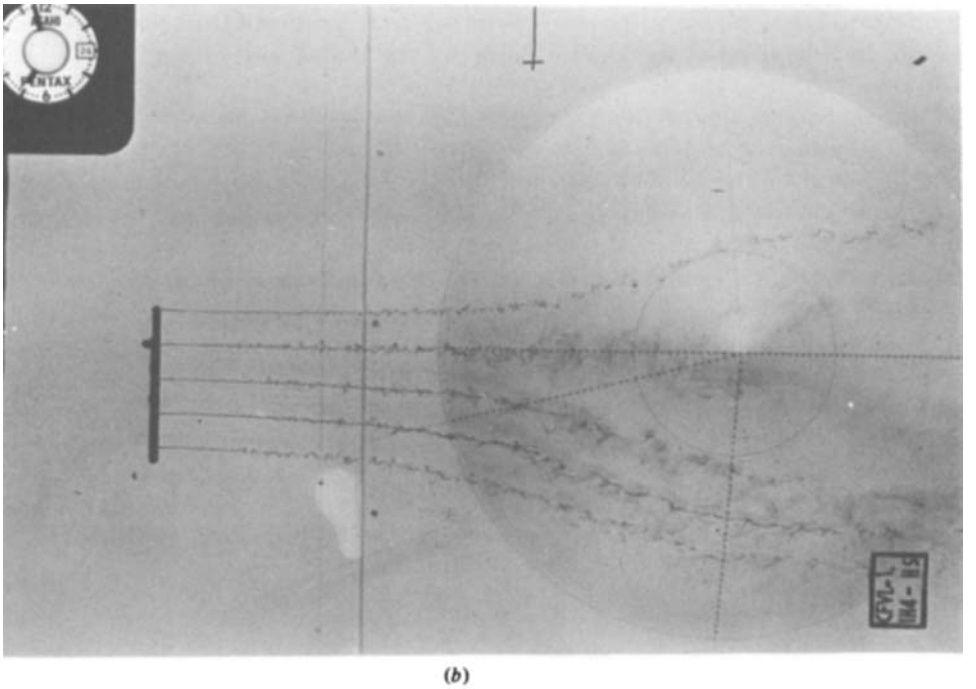

(*b*)

FIGURE 18. Top-view photographs of horizontal-rake plume release for the case $h^* = 2.0$: (*a*) $F_0 = 0.71$; (*b*) $F_0 = 1.4$. Rake is at half the interface height.

clearly demonstrated plume impingement on the obstacle. At $F_0 \leqslant 0.85$ all the lower-layer plumes impinge on the hill surface and bifurcate, while upper-layer plumes clear the crest. All the plumes clear the crest of the hill at $F_0 = 1.41$. Experiments for $h^* = 2.0$ were also repeated with a horizontal rake at an elevation of half the interface height. The results (see figures 16*a*, *b*) clearly show plume impingement on the hill at low Froude numbers and the plumes rising over the crest at large Froude numbers.

4. Conclusions

A numerical model of the shallow-water equations was used to demonstrate that the three-dimensionality of an obstacle and resultant flow around causes a shift of the analytically derived curve separating steady subcritical from critical flow for a two-dimensional ridge. This effect is predictably enhanced as the cross-stream obstacle width is decreased, but the criterion for change of regime retains its dependence on the two parameters F_0 and h^*. Of the two measures suggested for quantitatively describing the relative deflection, the first, based on the cross-sectional mass-flux distribution, is the more precise, but based on information not readily available in laboratory or field experiments. The second measure, based on a graphical determination of deflection of streamlines, is less rigorous but more readily adaptable to atmospheric data.

The laboratory experiments have demonstrated that the flow regimes predicted by the numerical solutions of the time-dependent model for a three-dimensional obstacle correspond well qualitatively with those that occur in a real fluid, although the phenomenon of separation and wave effects in the lee introduce important differences. For values of $h^* \geqslant 1$ the occurrence of interface impingement was demonstrated to occur for values of F_0 less than that predicted by a criterion derived through consideration of the kinetic energy of the initial flow.

The authors were financially supported through appointments at North Carolina State University under U.S. E.P.A. cooperative agreement R805595. The authors would like to thank Dr S. P. S. Arya for his support and encouragement throughout the project. The second author gratefully acknowledges the help of Messrs Leonard Marsh and Lee Griffin for help in carrying out the laboratory experiments and processing the photographs. Appreciation is also due to Dr William Snyder and the staff of the Fluid Modeling Facility for their cooperation and help in the planning and conduct of experiments. Appreciation is also due to Dawn Abatemarco and Brenda Batts for a fine typing job, and to Toni Clay and Pat Bowers for the excellent drafting.

REFERENCES

Arakawa, A. & Lamb, V. R. 1977 Computational design of the basic dynamical processes of the UCLA General Circulation Model. *Meth. Comp. Phys.* **17**, 173–265.

Baines, P. G. & Davies, P. A. 1980 Laboratory studies of topographic effects in rotating and/or stratified fluids. In *Orographic Effects in Planetary Flows*, chap. 8. WMO GARP Publication 23.

Houghton, D. D. & Kasahara, A. 1968 Nonlinear shallow fluid flow over an isolated ridge. *Commun. Pure Appl. Maths* **21**, 1–23.

Hunt, J. C. R. & Snyder, W. H. 1980 Experiments on stably and neutrally stratified flow over a model three-dimensional hill. *J. Fluid Mech.* **96**, 671–704.

LARSEN, L. H. 1966 Flow over obstacles of finite amplitude. *Geofys. Publ.* **26**, 1–25.

LILLY, D. K. 1965 On the computational stability of numerical solutions of time-dependent non-linear geophysical fluid dynamics problems. *Mon. Weath. Rev.* **93**, 11–26.

LONG, R. R. 1954 Some aspects of the flow of stratified fluids. II. Experiments with a two-fluid system. *Tellus* **6**, 97–115.

LONG, R. R. 1972 Finite amplitude disturbances in the flow of inviscid rotating and stratified fluids over obstacles. *Ann. Rev. Fluid Mech.* **4**, 69–92.

MESINGER, F. & ARAKAWA, A. 1976 *Numerical Methods used in Atmospheric Models.* WMO GARP Publication 17.

OOBAYASHI, T. 1970 A numerical study of two-dimensional airflow over an isolated mountain. *J. Met. Soc. Japan* **48**, 118–127.

SNYDER, W. H., BRITTER, R. E. & HUNT, J. C. R. 1979 A fluid modeling study of the flow structure and plume impingement on a three-dimensional hill in stably stratified flow. In *Proc. Intl Conf. on Wind Engng, Fort Collins, Colorado.*

STOKER, J. J. 1957 *Water Waves.* Interscience.